EDGE ARTICLE

Check for updates

CO$_2$-broken Ti–O bonds in the TiO$_6$ octahedron of CaTiO$_3$ for greatly enhanced room-temperature ferromagnetism†

Yuqi Ouyang,‡[a] Bo Gao,‡[a] Yaozheng Tang,[a] Lianyu Li[a] and Qun Xu ⓘ *[ab]

Preparation of two-dimensional (2D) ferromagnetic nanomaterials and the study of their magnetic sources are crucial for the exploration of new materials with multiple applications. Herein, two-dimensional room-temperature ferromagnetic (FM) CaTiO$_3$ nanosheets are successfully constructed with the assistance of supercritical carbon dioxide (SC CO$_2$). In this process, the SC CO$_2$-induced strain effect can lead to lattice expansion and introduction of O vacancies. More importantly, experimentally it can be found out that the breakage of the Ti–O$_2$ bond by CO$_2$ directly results in the equatorial plane of the TiO$_6$ octahedron being exposed. This leads to more opportunities for oxygen vacancies and low-valent titanium to appear, where Ti^{3+} can optimize the spin structure, releasing the macroscopic magnetization. Greatly improved room-temperature ferromagnetic behavior, with an optimal magnetization of 0.1661 emu g^{-1} and a high Curie temperature (Tc) of 300 K can be achieved.

Introduction

With the advancement of nanotechnology, magnetic nanomaterials have shown great potential in magnetic recording and data storage due to their unique physical properties.[1–3] Two-dimensional magnetic nanomaterials have attracted increasing research interest for fundamental physical studies as well as their huge potential applications in spintronic devices such as magnetic tunnel junctions, spin tunnel field-effect transistors, and spin valves.[4–6] 2D room-temperature ferromagnetic materials offer substantial potential for various advanced technological applications, particularly in fields like microelectronics, spintronics, non-volatile memory, and sensor technologies, and the discovery of ferromagnetism at room temperature in two-dimensional materials provides new possibilities for next-generation low-power, high-density electronic and information storage devices.[7,8]

Among the plethora of magnetic materials discovered, perovskite oxides stand out for their intriguing array of physical properties, including ferroelectricity, ferromagnetism, superconductivity, and magnetoresistance, and this multifaceted behavior has sparked a surge of interest in both fundamental and applied investigations, leading to a significant global research endeavor over the past few decades.[9–11] The robust correlation between the atomic structure and magnetic properties has been well documented in bulk perovskites.[12,13] The general chemical formula for a chalcogenide oxide is ABO$_3$, with A being the larger cation that forms the cubic sublattice and B being the smaller cation that is body-centered and cubic; in most cases, the B ion is coordinated with six O^{2-} anions in corner-connected BO$_6$ octahedra.[14] Epitaxial strain can have a profound effect on the BO$_6$ bonding environment, resulting in BO$_6$ distortion and/or rotations.[15,16] Given that magnetic ordering and transition temperatures in perovskites are sensitive to the B–O lengths and the B–O–B angles, modifying octahedral distortions and rotations provides a means of engineering magnetism in perovskite oxides.[17] Furthermore, extrinsic effects such as oxygen vacancies, local non-stoichiometry, and cation intermixing are always present to some degree at real interfaces, and in some cases these effects dominate magnetic behavior.[18–21] Nevertheless, the current development of spintronic devices is still hindered by limitations in both mechanisms and suitable materials. Finding stable two-dimensional ferromagnetic materials with room-temperature Curie temperatures and investigating their magnetic modulation mechanisms are key scientific issues for the development of spintronic devices, but challenges remain.

As a typical perovskite oxide, CaTiO$_3$ is of great interest due to its high dielectric constant, low dielectric losses, and wide band gap.[20] In the field of ferromagnetism, Hosseini prepared CaTiO$_3$ nanoparticles by the sol–gel method, which exhibits room-temperature ferromagnetism after calcination at high temperature in air.[22] Sun *et al.* found that room temperature ferromagnetism is present in the nanocrystalline CaTiO$_3$ plates

[a]*College of Materials Science and Engineering, Zhengzhou University, Zhengzhou 450052, P. R. China. E-mail: qunxu@zzu.edu.cn*

[b]*Henan Institute of Advanced Technology, Zhengzhou University, Zhengzhou 450052, P. R. China*

‡ These authors contributed equally to this work.

© 2025 The Author(s). Published by the Royal Society of Chemistry

that are annealed at 1000 °C for 1 h and reduces after vacuum annealing, suggesting that the room temperature FM originates from the cation vacancies.[23] Xu *et al.* reported that the spontaneous formation of a hole polaron in $CaTiO_3$ could induce the coexistence of ferroelectricity and magnetism.[24]

In contrast to conventional techniques, SC CO_2 displays superior capabilities in the synthesis and optimization of room-temperature ferromagnetic materials,[25,26] owing to its excellent performance, such as high diffusion coefficients, outstanding wetting of surfaces, and low interfacial tension.[27,28] In this work, we report SC CO_2-assisted fabrication of 2D $CaTiO_3$ nanosheets. In the presence of SC CO_2, bulk $CaTiO_3$ was exfoliated into nanosheet layers. The strain effect of SC CO_2 at different pressures induces modulation and selective breakage of covalent bonds, which leads to the specific surface exposure of the prepared 2D $CaTiO_3$. This results in an increase in the concentration of O vacancies and Ti^{3+}, inducing 2D $CaTiO_3$ to exhibit room-temperature ferromagnetism ($Tc = 300$ K). The saturation magnetization (Ms) value of 2D $CaTiO_3$ is 0.1661 emu g^{-1}, which is 32 times higher than that of the pristine $CaTiO_3$ prepared by the sol–gel method.[22]

Results and discussion

Structural characterization of $CaTiO_3$

Two-dimensional layered $CaTiO_3$ nanosheets were prepared from pristine $CaTiO_3$ powder with the aid of SC CO_2 (Fig. 1a), and the preparation details are shown in the ESI.† The effect of SC CO_2 in $CaTiO_3$ is shown in Fig. 1b, where CO_2 carries external physical pressure into the crystal structure, stretching the TiO_6 octahedra, producing strain effects, destroying the original chemical coordination, exposing (101) the crystal plane and forming localized defects.
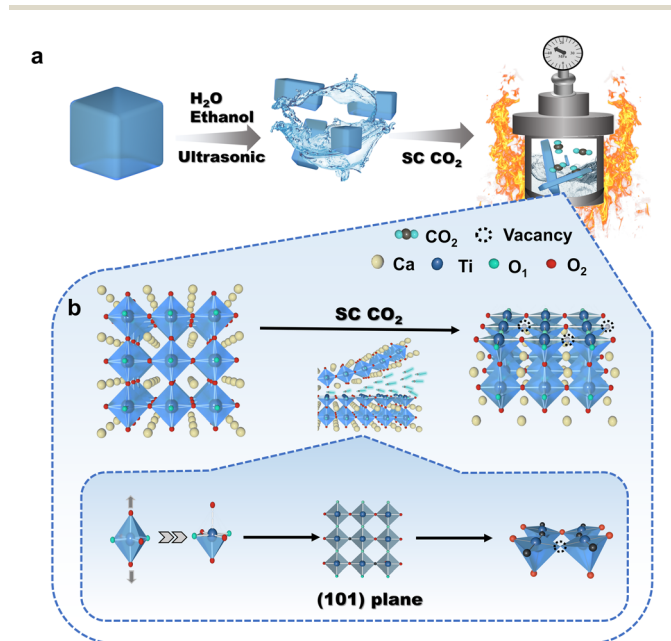
The samples were observed by atomic force microscopy (AFM), and it was found that the SC CO_2-treated 2D $CaTiO_3$ nanosheets had a thickness of approximately ≈ 3.65 nm (Fig. 2a and b). The statistical analysis based on the AFM measurements demonstrated that the $CaTiO_3$ nanosheets had various thicknesses, while 6–10 layers were found to be the major components (73.68%) (Fig. S2†).

To obtain information on the microscopic morphology and structure, the samples were observed by transmission electron microscopy (TEM), and the images (Fig. 2c and S3†) also verified the low-layer $CaTiO_3$ nanosheets, which turned slightly transparent to the electron beam. The atomic arrangement was characterized using high-resolution TEM (HRTEM) images and Fast Fourier transform (FFT) analysis. As shown in Fig. 2d, the lattice spacings of the SC CO_2-treated $CaTiO_3$ at 16 MPa are 0.384 and 0.273 nm, respectively, which are similar to the $(10\bar{1})$ and $(12\bar{1})$ lattice spacings of standard $CaTiO_3$ (0.382 and 0.272 nm), but with a slight increase, suggesting an increase in the lattice spacings of $CaTiO_3$ after the SC CO_2 treatment. Since SC CO_2 has been reported to induce strain effects in oxide perovskites, we performed geometric phase analysis (GPA) on HRTEM images to assess the lattice strain of $CaTiO_3$.[29] The diffraction points $(10\bar{1})$ and $(0\bar{2}0)$ in the inset of Fig. 2d were considered as the reflection sets. The strain effect of $CaTiO_3$ nanosheets can be observed in Fig. 2f. Subsequently, the variation in strain was confirmed along the y-axis (ε_{yy} in Fig. S8, ESI†). The strain maps illustrate that lattice strain existed in
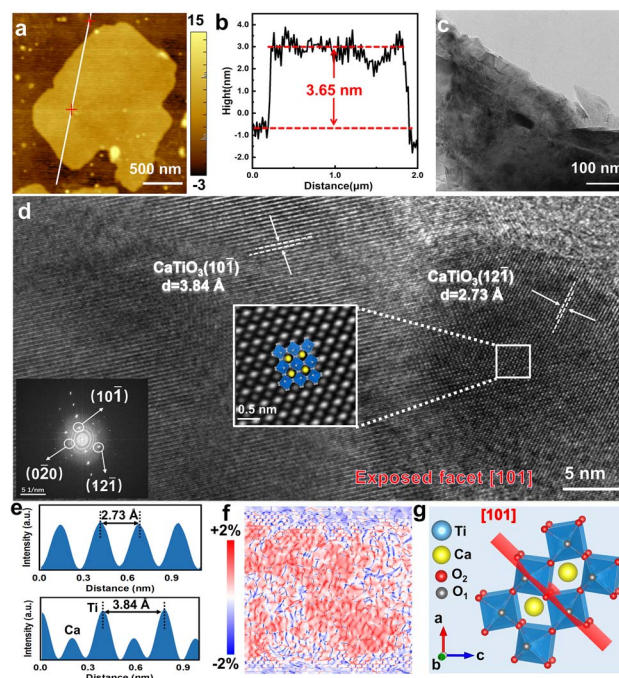

Fig. 1 (a) The process flow of SC CO_2 stripping on bulk phase $CaTiO_3$. (b) Schematic diagram of the effect of SC CO_2 on $CaTiO_3$.

Fig. 2 Characterization of $CaTiO_3$ nanosheets treated with SC CO_2 at 16 MPa. (a) AFM image and (b) height profile of the line in (a). (c) TEM image. (d) HRTEM image. (e) The line contour of the plane spacing in (d). (f) The strain map demonstrate on the HRTEM image by geometric phase analysis (GPA). Strain-values from −2% to +2% can be represented when color changes from blue to red. (g) Atomic structure diagram of the (101) plane.

$CaTiO_3$ after the SC CO_2 treatment. Moreover, the FFT-filter atomic resolution image is further utilized to visualize the domain transformation of the white-boxed region in Fig. 2d, and by fitting with the crystal models, the exposed surface of $CaTiO_3$ at this pressure was determined to be the (101) crystal surface.

The crystal structures of the as-prepared nanosheets were examined using X-ray diffraction (XRD), as shown in Fig. 3. The characteristic peaks for all samples matched well with the orthorhombic structure of $CaTiO_3$ (PDF card no. 22-0153, space group *Pnma*). Meanwhile, partially enlarged details of the (101), (121), and (042) planes (Fig. 3b) indicate that the diffraction peak of $CaTiO_3$ after SC CO_2 treatment shifted toward a lower angle, which is essential evidence for the increased lattice spacing originated from the strain effect due to the SC CO_2 treatment, as observed by TEM characterization. The Williamson–Hall method was used to calculate the micro-strains in the samples, and the results are shown in Fig. S9,† which indicate that different strains can be obtained upon pressure variation.[30] The degrees of sample strain at different pressures indicate that CO_2 at a pressure of 16 MPa exerts the most significant influence on the strain effect of $CaTiO_3$, which reaches 1.324%. Furthermore, the Bragg equation was employed to calculate the increased proportion of the lattice spacings and lattice constants (Tables 1 and S1†). Notably, the largest increase in lattice spacing corresponding to the (101) plane was ≈1.5313%, suggesting that the (101) crystal plane may be more susceptible to being stretched.

To obtain more structural information on $CaTiO_3$ crystals under the strain effect, the GSAG II & EXPGUI software was used for Rietveld refinement analyses based on the XRD patterns of the sample under SC CO_2 treatment. As shown in Fig. 3c, the reliability factor of the weighted patterns (R_{wp}) was less than

Table 1 The lattice spacing and stretching ratio of different planes in $CaTiO_3$ treated with SC CO_2 at 16 MPa

Plane	Standard D (nm)	D (nm)	Δd (nm)	Strain%
(101)	3.8240	3.8826	0.0586	1.5313
(121)	2.7010	2.7298	0.0288	1.0649
(040)	1.9110	1.9216	0.0106	0.5552
(042)	1.5570	1.5635	0.0065	0.4132

10%, indicating the high credibility of the fitting results. The results of the refinement demonstrate that as the CO_2 pressure increases, the coordination environment of Ti ([TiO_6] octahedra) was significantly distorted, including an increase in the average bond length, octahedral volume, and distortion index (Table S2†).

In the case of an octahedron centered on a Ti atom, the Ti atom is bonded to six neighboring O atoms. Two distinct types of Ti–O bonds are established, featuring varying bond lengths.[31] The shorter bond is denoted as Ti–O_1, with a length of 1.9508 Å, while the longer bond is referred to as Ti–O_2, with a length of 1.9572 Å.[32] In the refinement results, the Ti–O_2 bond was observed to undergo a greater degree of stretching than the Ti–O_1 bond when subjected to the same SC CO_2 pressure (Fig. 3d). This phenomenon can be attributed to the inverse relationship between bond length and interatomic interactions, whereby longer bond lengths result in weaker interatomic forces. At a CO_2 pressure of 16 MPa, there was a notable increase in the Ti–O_2 bond length. Furthermore, at 16 MPa, the crystal surface exposed in $CaTiO_3$ is the (101) crystal surface, and both Ti–O_1 and Ti–O_2 are present in the plane. However, only Ti–O_2 is perpendicular to the direction of the (101) crystal surface, which is out of the plane. This difference between the in-plane and out-of-plane directions is also the reason for the different degrees of stretching of the two bonds.[32] Given that the bond length is inversely proportional to the strength of interatomic interactions, this expansion in the Ti–O_2 bond length resulted in a corresponding weakening of the interactions between Ti and O_2 atoms. Consequently, the Ti–O_2 bonds were more susceptible to breakage when external factors were introduced to create exposure of (101) crystal surfaces, which aligns with the observations reported in the HRTEM results.

The composition and chemical state of the as-prepared $CaTiO_3$ were characterized by X-ray photoelectron spectroscopy (XPS) as shown in Fig. 4 and S11†. Fig. 4a illustrates that the Ti $2p_{1/2}$ and Ti $2p_{3/2}$ XPS lines of $CaTiO_3$ exhibit two peaks at 463.90 and 458.06 eV, respectively, under a range of experimental conditions, including SC CO_2 treatment and ultrasonic treatment, and these peaks are attributed to the Ti^{4+} in $CaTiO_3$.[33] Following SC CO_2 treatment, the Ti 2p XPS lines exhibited two additional characteristic peaks centered at 458.09 and 457.58 eV (red area), which were attributed to Ti^{3+}.[34,35] The XPS spectrum of O is shown in Fig. 3b. The O 1s spectrum of pristine $CaTiO_3$ is deconvoluted into four peaks. The peak at 529.49 eV is ascribed to the crystal lattice oxygen (O_L), the peak at 530.53 eV is attributed to the oxygen vacancy (O_V) (red area),
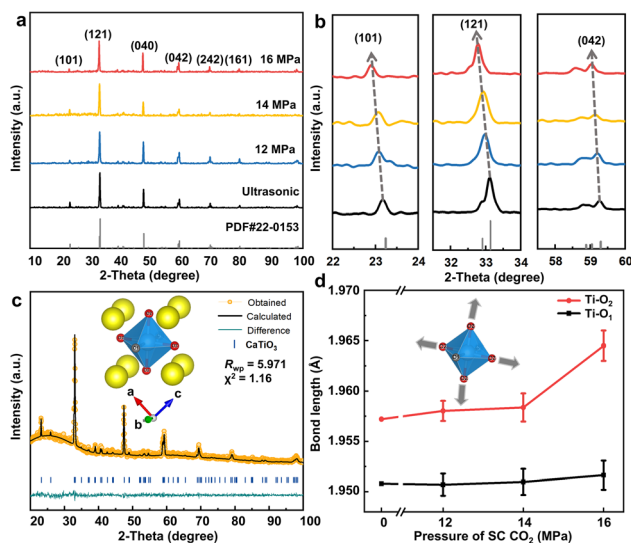
Fig. 3 Characterization of $CaTiO_3$ under different pressure treatments. (a) XRD. (b) Partially enlarged details of some planes. (c) The Rietveld-refined XRD patterns of $CaTiO_3$ under 16 MPa. (d) Variation in the bond length value of TiO_6 octahedra obtained by XRD refinement with increasing SC CO_2 pressure.
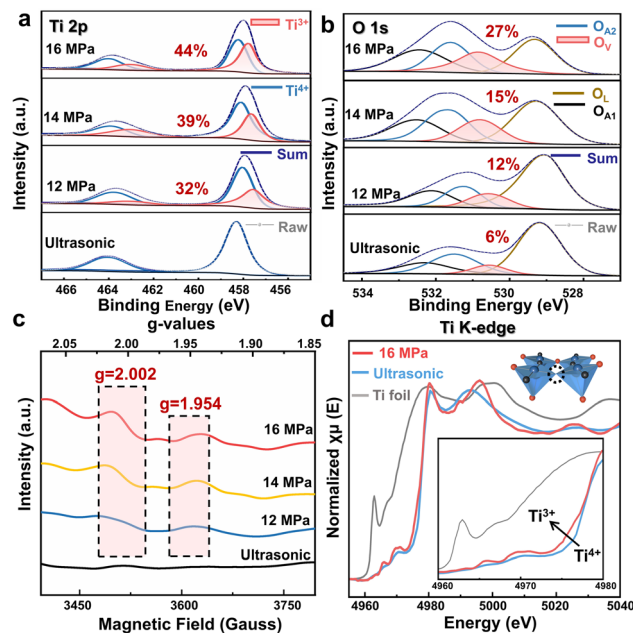
Fig. 4 High-resolution XPS characterization under different CO_2 pressures. (a) Ti 2p. (b) O 1s. The percentage in Fig. 4a and b corresponds to the content of Ti^{3+} and O_v, respectively. (c) Cryo-electron paramagnetic resonance (EPR) spectra. (d) Ti K-edge XANES spectra of Ti foil and $CaTiO_3$ under different treatments. (Inset) A schematic diagram of the formation of the O-vacancy in non-stoichiometric $CaTiO_3$ under the treatment with SC CO_2 at 16 MPa. The blue balls represent Ti atoms, the red balls represent O_1 atoms, the black balls represent O_2 atoms, and the dashed circle represents the oxygen vacancy.

the peak at 531.27 eV is attributed to OH^- and CO_3^{2-} groups (O_{A2}) and the peak at 532.2 eV is attributed to the surface adsorbed oxygen (O_{A1}).[35–37]

According to Fig. S11,† the two peaks at 349.87 and 346.43 eV in the Ca $2p_{1/2}$ and Ca $2p_{3/2}$ XPS lines of $CaTiO_3$ are attributed to the Ca^{2+} in $CaTiO_3$.[38] After SC CO_2 treatment, two new characteristic peaks emerged at 355.49 and 346.96 eV (red area), which are assigned to the Ca at the surface, such as $CaCO_3$ and Ca $(OH)_2$.[36]

Low-temperature electron paramagnetic resonance (EPR) of the $CaTiO_3$ samples is shown in Fig. 4c. After the SC CO_2 treatment, a signal appears at approximately $g = 2.002$, which is assigned to the electrons trapped in the O_V. Moreover, $CaTiO_3$ treated with SC CO_2 exhibits a signal at $g = 1.954$, which can be attributed to the d^1 electron of Ti^{3+}.[39–41] The appearance of these two signal peaks further confirms the effect of the SC CO_2 pressure on the surface O_Vs and Ti^{3+} concentration, which is in line with the XPS studies.

In order to elucidate the local order structure around the Ti atom, Ti K-edge X-ray absorption near-edge structure (XANES) spectra were measured. As illustrated in Fig. 4d, the red curve (16 MPa SC CO_2 treated $CaTiO_3$) exhibits a slightly higher absorption intensity near the Ti^{3+} peak in comparison to the blue curve (Ultrasonic). This suggests that high-pressure synthesis may result in a greater extent of Ti^{4+} being partially reduced to Ti^{3+} in $CaTiO_3$, which is in accordance with the XPS

analysis (Fig. 4a).[42,43] Furthermore, the physical origin of the pre-edge feature at approximately 4965 eV is the transition of the metallic 1s electron to an unfilled d state.[34] This peak area was attributed to the five-fold coordination (TiO_5) concentration, and as shown in Fig. 4c, the area of this peak was observed to vary with the pressure of SC CO_2, indicating that the $CaTiO_3$ sample synthesized under high pressure may have undergone a crystal restructuring process, accompanied by an increase in the TiO_5 content, which could affect the overlap of Ti and O orbitals.[44,45] Moreover, the intensity of first features beyond the edge (between 4980 and 5010 eV) is observed to increase with the increase in pressure of CO_2. The higher intensity of these peaks indicates that the local environment of the Ti atom is non-centrosymmetric, which distorts the octahedral configuration.[46,47] It has been established that oxygen vacancies play a crucial role in the ferromagnetic ordering of otherwise non-magnetic materials, whereby they facilitate carrier-mediated ferromagnetic interactions between Ti ions.[45] In the case of $CaTiO_3$, the presence of oxygen vacancies has been observed to promote spin-polarized charge carriers, thereby enhancing the overall magnetic moment of the material.

It is evident that the concentration of Ti^{3+} and O_V are elevated upon the introduction of SC CO_2, which corroborates the presence of defects in the SC CO_2 treated $CaTiO_3$ samples. These defects resulted in the formation of non-stoichiometric $CaTiO_3$. A substantial body of previous studies has demonstrated a robust correlation between non-stoichiometry and material magnetism. A comparison of the variation of Ti^{3+} and O_V with SC CO_2 pressure revealed that the O_V and Ti^{3+} contents reached their maximum values at 16 MPa (Fig. S12†), which may be related to the exposure surface. The breakage of the $Ti-O_2$ bond, which occurs when the (101) crystalline surface of $CaTiO_3$ is exposed, results in the equatorial plane of the TiO_6 octahedron being exposed. This leads to an increase in the occupation of Ti and O atoms on the surface, thereby increasing the probability of the formation of Ti^{3+} and O_V.

Magnetic properties

The magnetic properties of the as-obtained 2D $CaTiO_3$ were subsequently investigated by using a SQUID magnetometer. The ferromagnetic nature was confirmed by the appearance of magnetic hysteresis, saturation magnetization (Ms), and coercivity (Hc). Compared to the combination of ferromagnetism and diamagnetism of ultrasonicated $CaTiO_3$ in Fig. 5a, CO_2-treated $CaTiO_3$ exhibited significantly enhanced ferromagnetism with saturation magnetizations of 0.1611, 0.0603, and 0.0229 emu g^{-1}, respectively (Fig. 5b). This value is higher than that in previously reported $CaTiO_3$ nanoparticles prepared by the sol–gel method (0.005 emu g^{-1}) or the high-temperature solid-phase synthesis method (0.13 emu g^{-1}).[22,23] The enlarged part of the curve near $H = 0$ (Fig. 5c) shows an obvious residual magnetization (0.0117 emu g^{-1}) and coercive field (71.44 Oe). Additionally, the room-temperature ferromagnetic signature of the $CaTiO_3$ nanosheets with SC CO_2 treatment was validated by analyzing the temperature dependence of magnetization measurements. Under a constant magnetic field ($H = 500$ Oe),
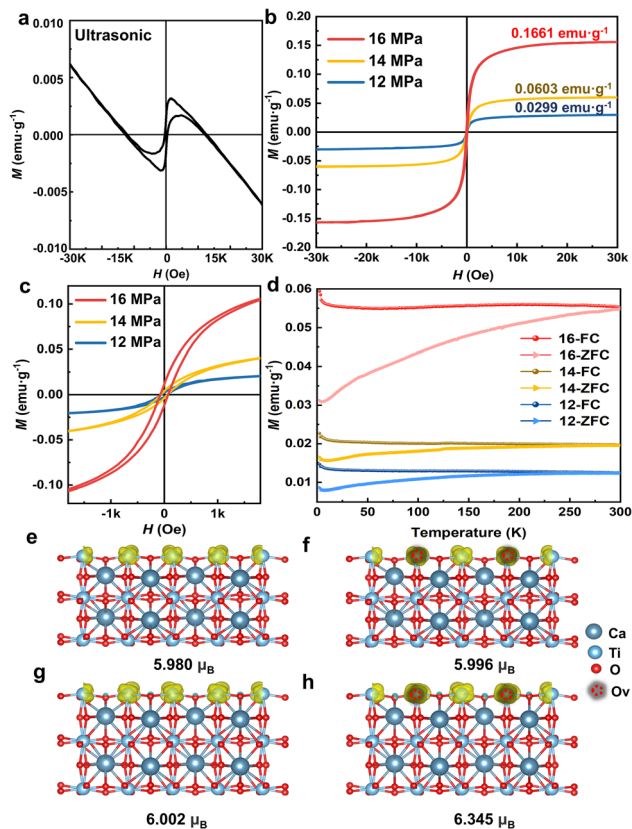
Fig. 5 Ferromagnetic behavior. (a and b) $M–H$ curves at 300 K. (c) Magnified curves near $H = 0$ Oe. (d) FC-ZFC magnetization curve of CaTiO$_3$ treated with SC CO$_2$ in an external magnetic field of 500 Oe. (e) Spin charge density distribution of the (101) plane without the strain effect or oxygen vacancies. (f) Spin charge density distribution with oxygen vacancies. (g) Spin charge density distribution with the strain effect. (h) Spin charge density distribution with the strain effect and oxygen vacancies.

field cooling (FC) and zero-field cooling (ZFC) processes were applied to measure the temperature dependence of magnetization ($M–T$) from 5 to 300 K (Fig. 5d). The FC magnetization curve exhibited a downward trend during heating, whereas the ZFC magnetization curve increased with increasing temperature. Importantly, the FC and ZFC lines intersected at approximately 300 K, indicating that the transition temperature of the sample was approximately room temperature. Because no magnetic impurities were observed according to the XPS survey (Fig. S13†), it can be concluded that the observed room-temperature ferromagnetism originates from the CaTiO$_3$ sample under SC CO$_2$ treatment. Furthermore, following a one-year period of storage at room temperature and pressure, the $M–H$ curve was reassessed, and the results are shown in Fig. S14;† these results demonstrate that Ms of the samples exhibited only minor reductions, confirming the robust stability of ferromagnetism in SC CO$_2$-induced ferromagnetic CaTiO$_3$.

In order to investigate the origin of room-temperature ferromagnetism in SC CO$_2$-treated CaTiO$_3$, density-functional theory (DFT) calculation was conducted. According to experimental results, the breakage of Ti–O$_2$ bonds in the TiO$_6$

octahedra and the exposure of (101) facets occurred in SC CO$_2$-treated CaTiO$_3$ as a consequence of strain effects. These strain effects, induced by lattice distortions, can significantly modify magnetic interactions by altering the electronic structure, bond lengths and orbital overlap.[48,49] Moreover, experimental results reveal that oxygen vacancies in CaTiO$_3$ are generated in conjunction with the strain effect. Numerous studies on perovskite oxide have established that oxygen vacancies can disrupt the local electronic structure and generate unpaired electron spins, leading to localized magnetic moments.[21,50] Consequently, the spin charge density distributions of the (101) plane in CaTiO$_3$ were modelled using DFT, with a focus on separately investigating the effects of oxygen vacancies and tensile strain to ascertain which factor exerts a more dominant influence on the magnetic properties of CaTiO$_3$. As illustrated in Fig. 5e, the magnetic moment of CaTiO$_3$ without oxygen vacancies or tensile strain was 5.980 μ_B. Upon the introduction of oxygen vacancies and tensile strain, the magnetic moment increased to 5.996 μ_B and 6.002 μ_B, respectively (Fig. 5f and g). It is evident that tensile strain has a more pronounced impact on the magnetic properties of CaTiO$_3$ than the presence of vacancies. Furthermore, according to the calculations, the magnetic moment of the (101) plane in CaTiO$_3$ increases by 6% to 6.354 μ_B as a result of the combined effect of oxygen vacancies and tensile strain. However, due to the limitation of the number of atoms (eight CaTiO$_3$ formula units), the promotion of CaTiO$_3$ ferromagnetism by the surface strain effect and oxygen vacancies is constrained during the calculation. In contrast, experimental evidence demonstrates that there is a considerably larger amount of surface strain effect and defect content in the SC CO$_2$-treated CaTiO$_3$. Nevertheless, the calculation results still indicate that on the basis of surface formation, the presence of oxygen vacancies and strain has a further enhancing effect on the observed ferromagnetism. Therefore, based on both experimental and theoretical investigations, the origin of ferromagnetism in CaTiO$_3$ can be attributed to the combined effect of strain and oxygen vacancies induced by surface exposure during SC CO$_2$ treatment.

Experimental

Materials

Commercial CaTiO$_3$ powder (99%) was purchased from Sigma Aldrich and can be used without further purification, and 99.99% pure CO$_2$ was provided by Zhengzhou Shuang yang Gas Company as the receiver. All the experimental ethanol was purchased from China Medical Chemical Reagent Co., Ltd, and deionized water was prepared with double-distilled water.

Exfoliation process

The SC CO$_2$ apparatus used for this experiment was composed mainly of a stainless steel autoclave (50 mL) with a heating jacket and a temperature controller. In this study, 60 mg bulk CaTiO$_3$ was dispersed in 30 mL of ethanol/water ($V_{ethanol} : V_{water}$ = 1 : 1) solution and subjected to ultrasonic treatment for 4 hours. The resulting suspension was labeled as ultrasonicated

$CaTiO_3$. Meanwhile, the autoclave was heated up to 40 °C. Then the ultrasonicated $CaTiO_3$ was immediately transferred into the autoclave, and CO_2 was subsequently charged into the autoclave to the desired pressure (12/14/16 MPa) under stirring. During the exfoliation process, the temperature and pressure of the autoclave were kept constant. After reaction for 4 hours under SC CO_2 conditions, the system was slowly depressurized and the sample was collected. The resulting dispersion was centrifuged at 4500 rpm for 10 minutes to remove the aggregates, and the precipitated supernatant was collected at 10 000 rpm for 15 minutes. Finally, the precipitates were dried in an oven at 60 °C.

Characterization

Transmission electron microscope (TEM) images were recorded on a FEI Tecnai G2-F20 at an acceleration voltage of 200 kV. The thickness of nanosheets was measured by using an atomic force microscope (Bruker Dimension Icon). X-ray diffraction (XRD) patterns were collected on a Bruker D8 Focus diffractometer (Bruker AXS, Germany) using Cu K radiation. X-ray photoelectron spectroscopy (XPS) was performed using a Thermo Scientific K-Alpha+ system. Raman measurements were performed using a LabRAM HR Evolution with a laser wavelength of 830 nm. The electron paramagnetic resonances were obtained by using an electron paramagnetic resonance spectrometer (EMX-9.5/12). The magnetic measurement was carried out with a physical property measurement system (quantum design, PPMS-9) and the magnetic hysteresis loop is obtained in the range of $-30k$ Oe $< H < 30k$ Oe at room temperature. K-edge analysis was performed with Si(111) crystal monochromators at the BL11B beamlines at the Shanghai Synchrotron Radiation Facility (SSRF) (Shanghai, China). Before the analysis at the beamline, the samples were pressed into thin sheets 1 cm in diameter and sealed using a Kapton tape film. The XAFS spectra were recorded at room temperature using a 4-channel Silicon Drift Detector (SDD) Bruker 5040. Negligible changes in the line-shape and peak position of K-edge XANES spectra were observed between two scans taken for a specific sample. The spectra were processed and analyzed by the software codes Athena.[51]

Computational methods

The theoretical calculation based on density functional theory was completed by the VASP software package,[52] and the projector augmented wave (PAW) method[53] was used to describe the ion–electron interaction. Furthermore, the Perdew–Burke–Ernzerhof (PBE) functional[54] was used to describe the exchange–correlation energy of the simulation system, and DFT-D3[55] was used to improve the calculation accuracy of dispersion force. The cutoff energy of plane wave basis was 500 eV, and the Monkhorst Pack scheme was used to generate k-points with a density of 0.4 per Angstrom for Brillouin zone sampling. The self-consistent field (SCF) calculation was kept within the energy convergence criterion of 1.0×10^{-5} eV. EDIFFG: this parameter is used to control the force convergence criteria for structural optimization. The optimization ends when the force on all atoms is less than 0.01 eV $Å^{-1}$. In addition,

a correction based on the Hubbard U model was used for the d orbitals of Ti atoms to obtain more accurate correlation energy, and the U value was 3.4 eV. For the slab model,[56] a vacuum layer with a thickness of 15 Å was established to avoid layer-to-layer interaction.

The data obtained by XRD were imported into Origin software, and then the diffraction peak 2θ values of (121) (040) (042) were obtained by Lorentz fit. The Brag eqn (1) was used to obtain the plane spacing, and the Williamson–Hall (W–H) eqn (2) was used to calculate the strain.

$$d = \frac{n\lambda}{2\sin\theta} \qquad (1)$$

where $n = 1$ and $\lambda = 1.5406$ Å.

$$\beta\cos\theta = \frac{k\lambda}{D} + 4\sin\theta \qquad (2)$$

where β represents the full width at half maxima (FWHM). $k = 0.9$ and $\lambda = 1.5406$ Å.

Geometric Phase Analysis (GPA) of HRTEM images used the GMS plug-in FRWR tools.

Conclusions

In summary, 2D $CaTiO_3$ with room-temperature ferromagnetism has been prepared using SC CO_2. Experimental studies have demonstrated the critical synergistic role of SC CO_2 induced strain effects and O vacancies in ferromagnetic manipulation. Specifically, GPA illustrates the presence of strain effects, and XRD confirms the increase in crystal spacing, in particular the elongation of the Ti–O_2 bonds in TiO_6 octahedron, and the breakage of the Ti–O_2 bonds at the surface of $CaTiO_3$ forms the exposition of (101) plane observed in HRTEM, which confers more opportunities for oxygen vacancies and low-valent titanium to appear, where Ti^{3+} can optimize the spin structure, releasing the macroscopic magnetization, which leads to weak ferromagnetic ordering. To the best of our knowledge, this is the first report of increasing the intrinsic magnetic properties of $CaTiO_3$ by an external stress field approach. This approach can achieve 2D ferromagnetism at room temperature Tc, in contrast to the conventional doping with magnetic impurities or building defects. Significantly, this method has been demonstrated to be effective in other perovskite,[26] offering a promising avenue for investigating room-temperature ferromagnetism in perovskite materials.

Data availability

The data supporting this article have been included as part of the ESI.†

Author contributions

Y. Ouyang conducted experiments, collected data and wrote the manuscript. B. Gao conducted computational investigations. Y. Tang and L. Li interpreted the data. Q. Xu designed the project and experiments.

Conflicts of interest

There are no conflicts to declare.

Acknowledgements

Notes and references

1 S. P. Gubin, Y. A. Koksharov, G. B. Khomutov and G. Y. Yurkov, *Russ. Chem. Rev.*, 2005, **74**, 489.

2 L. Cai, J. He, Q. Liu, T. Yao, L. Chen, W. Yan, F. Hu, Y. Jiang, Y. Zhao, T. Hu, Z. Sun and S. Wei, *J. Am. Chem. Soc.*, 2015, **137**, 2622.

3 Y. Sun, H. Lv, H. Yao, Y. Gao and C. Zhang, *Carbon Energy*, 2024, **6**, e575.

4 Q. H. Wang, A. Bedoya-Pinto, M. Blei, A. H. Dismukes, A. Hamo, S. Jenkins, M. Koperski, Y. Liu, Q.-C. Sun, E. J. Telford, H. H. Kim, M. Augustin, U. Vool, J.-X. Yin, L. H. Li, A. Falin, C. R. Dean, F. Casanova, R. F. L. Evans, M. Chshiev, A. Mishchenko, C. Petrovic, R. He, L. Zhao, A. W. Tsen, B. D. Gerardot, M. Brotons-Gisbert, Z. Guguchia, X. Roy, S. Tongay, Z. Wang, M. Z. Hasan, J. Wrachtrup, A. Yacoby, A. Fert, S. Parkin, K. S. Novoselov, P. Dai, L. Balicas and E. J. G. Santos, *ACS Nano*, 2022, **16**, 6960.

5 X. Zhang, X. Wang, T. He, L. Wang, W.-W. Yu, Y. Liu, G. Liu and Z. Cheng, *Sci. Bull.*, 2023, **68**, 2639.

6 Y. Jiao, Y. Li, Y. Zhou, P. Cen, Y. Ding, Y. Guo and X. Liu, *Chin. Chem. Lett.*, 2024, **35**, 109082.

7 Y. Guo, B. Wang, X. Zhang, S. Yuan, L. Ma and J. Wang, *InfoMat*, 2020, **2**, 639.

8 C. Gong, L. Li, Z. Li, H. Ji, A. Stern, Y. Xia, T. Cao, W. Bao, C. Wang, Y. Wang, Z. Q. Qiu, R. J. Cava, S. G. Louie, J. Xia and X. Zhang, *Nature*, 2017, **546**, 265.

9 N. C. Bristowe, J. Varignon, D. Fontaine, E. Bousquet and P. Ghosez, *Nat. Commun.*, 2015, **6**, 6677.

10 M. Namba, H. Takatsu, R. Mikita, Y. Sijia, K. Murayama, H.-B. Li, R. Terada, C. Tassel, H. Ubukata, M. Ochi, R. Saez-Puche, E. P. Latasa, N. Ishimatsu, D. Shiga, H. Kumigashira, K. Kinjo, S. Kitagawa, K. Ishida, T. Terashima, K. Fujita, T. Mashiko, K. Yanagisawa, K. Kimoto and H. Kageyama, *J. Am. Chem. Soc.*, 2023, **145**, 21807.

11 A. C. Garcia-Castro, Y. Ma, Z. Romestan, E. Bousquet, C. Cen and A. H. Romero, *Adv. Funct. Mater.*, 2022, **32**, 2107135.

12 P. G. Radaelli, G. Iannone, M. Marezio, H. Y. Hwang, S. W. Cheong, J. D. Jorgensen and D. N. Argyriou, *Phys. Rev. B:Condens. Matter Mater. Phys.*, 1997, **56**, 8265.

13 M. A. Subramanian, A. P. Ramirez and W. J. Marshall, *Phys. Rev. Lett.*, 1999, **82**, 1558.

14 H. Arandiyan, S. S. Mofarah, C. C. Sorrell, E. Doustkhah, B. Sajjadi, D. Hao, Y. Wang, H. Sun, B.-J. Ni, M. Rezaei, Z. Shao and T. Maschmeyer, *Chem. Soc. Rev.*, 2021, **50**, 10116.

15 A. Marthinsen, C. Faber, U. Aschauer, N. A. Spaldin and S. M. Selbach, *MRS Commun.*, 2016, **6**, 182.

16 Q. Wang, Y. Gu, C. Chen, L. Han, M. U. Fayaz, F. Pan and C. Song, *ACS Appl. Bio Mater.*, 2024, **16**, 3726.

17 J. M. Rondinelli, S. J. May and J. W. Freeland, *MRS Bull.*, 2012, **37**, 261.

18 S. Jaiswar and K. D. Mandal, *J. Phys. Chem. C*, 2017, **121**, 19586.

19 A. Bhattacharya and S. J. May, *Annu. Rev. Mater. Res.*, 2014, **44**, 65–90.

20 A. I. Waidha, H. K. Siddiqui, Y. Ikeda, M. Lepple, S. Vasala, M. Donzelli, A. D. Fortes, P. Slater, B. Grabowski, U. I. Kramm and O. Clemens, *Chem. Eur. J.*, 2021, **27**, 9763.

21 P. Tan, C. Zhu, J. Yang, S. Zhao, T. Xia, M.-H. Zhao, T. Han, Z. Deng and M.-R. Li, *Chin. Chem. Lett.*, 2024, **35**, 108485.

22 S. A. Hosseini, *J. Mater. Sci.:Mater. Electron.*, 2017, **28**, 3703.

23 L. Sun, Y. Zhang, L. Ju, C. Shi, H. Qin and J. Hu, *IEEE Trans. Magn.*, 2014, **50**, 1.

24 T. Xu, M. Mori, H. Hirakata, T. Kitamura and T. Shimada, *Phys. Chem. Chem. Phys.*, 2024, **26**, 842.

25 B. Gao, S. Xu and Q. Xu, *Angew. Chem., Int. Ed.*, 2022, **61**, e202117084.

26 L. Li, B. Gao, S. Xu and Q. Xu, *Small*, 2023, **19**, 2300765.

27 K. P. Johnston, K. L. Harrison, M. J. Clarke, S. M. Howdle, M. P. Heitz, F. V. Bright, C. Carlier and T. W. Randolph, *Science*, 1996, **271**, 624.

28 P. Zhou, Q. Xu, H. Li, Y. Wang, B. Yan, Y. Zhou, J. Chen, J. Zhang and K. Wang, *Angew. Chem., Int. Ed.*, 2015, **54**, 15226.

29 M. J. Hÿtch, E. Snoeck and R. Kilaas, *Ultramicroscopy*, 1998, **74**, 131.

30 B. L. Choudhary, U. Kumar, A. M. Quraishi, P. M. Z. Hasan, R. Darwesh, S. Kumar, S. Dalela, S. Kumar, S. N. Dolia and P. A. Alvi, *J. Mater. Sci.:Mater. Electron.*, 2022, **33**, 6829.

31 K. S. Knight, *J. Alloys Compd.*, 2011, **509**, 6337.

32 M. D. Biegalski, L. Qiao, Y. Gu, A. Mehta, Q. He, Y. Takamura, A. Borisevich and L.-Q. Chen, *Appl. Phys. Lett.*, 2015, **106**, 162904.

33 Y. Yan, H. Yang, X. Zhao, R. Li and X. Wang, *Mater. Res. Bull.*, 2018, **105**, 286.

34 G. K. Ribeiro, F. S. Vicente, M. I. B. Bernardi and A. Mesquita, *J. Alloys Compd.*, 2016, **688**, 497.

35 X. Zhang, L. Luo, R. Yun, M. Pu, B. Zhang and X. Xiang, *ACS Sustainable Chem. Eng.*, 2019, **7**, 13856.

36 S. Kačiulis, G. Mattogno, L. Pandolfi, M. Cavalli, G. Gnappi and A. Montenero, *Appl. Surf. Sci.*, 1999, **151**, 1.

37 T. Watanabe and T. Ohba, *Acs Sustain Chem Eng*, 2021, **9**, 3860.

38 J. Zhao, X. Cao, Y. Bai, J. Chen and C. Zhang, *Opt. Mater.*, 2023, **135**, 113239.

39 P. Boutinaud, E. Pinel, M. Dubois, A. P. Vink and R. Mahiou, *J. Lumin.*, 2005, **111**, 69.

40 M. Shivaram, R. H. Krishna, H. Nagabhushana, S. C. Sharma, B. M. Nagabhushana, B. S. Ravikumar,

N. Dhananjaya, C. Shivakumara, J. L. Rao and R. P. S. Chakradhar, *Mater. Res. Bull.*, 2013, **48**, 1490.

41 M. Shi, B. Rhimi, K. Zhang, J. Xu, D. W. Bahnemann and C. Wang, *Chemosphere*, 2021, **275**, 130083.

42 B. D. Begg, E. R. Vance, B. A. Hunter and J. V. Hanna, *J. Mater. Res.*, 1998, **13**, 3181.

43 L. R. Blackburn, L. T. Townsend, M. C. Dixon Wilkins, T. Ina, M. Kuman, S.-K. Sun, A. R. Mason, L. J. Gardner, M. C. Stennett, C. L. Corkhill and N. C. Hyatt, *Sci. Rep.*, 2023, **13**, 9329.

44 R. V. Vedrinskii, V. L. Kraizman, A. A. Novakovich, V. D. Ph and S. V. Urazhdin, *J. Phys.: Condens. Matter*, 1998, **10**, 9561.

45 S. A. Chambers, T. C. Droubay, C. M. Wang, K. M. Rosso, S. M. Heald, D. A. Schwartz, K. R. Kittilstved and D. R. Gamelin, *Mater. Today*, 2006, **9**, 28.

46 T. M. Mazzo, L. M. d. R. Oliveira, L. R. Macario, W. Avansi, R. S. Andre, I. L. V. Rosa, J. A. Varela and E. Longo, *Mater. Chem. Phys.*, 2014, **145**, 141.

47 S. de Lazaro, J. Milanez, A. T. de Figueiredo, V. M. Longo, V. R. Mastelaro, F. S. De Vicente, A. C. Hernandes, J. A. Varela and E. Longo, *Appl. Phys. Lett.*, 2007, **90**, 111904.

48 J. Wei, H. Zhong, J. Liu, X. Wang, F. Meng, H. Xu, Y. Liu, X. Luo, Q. Zhang, Y. Guang, J. Feng, J. Zhang, L. Yang, C. Ge, L. Gu, K. Jin, G. Yu and X. Han, *Adv. Funct. Mater.*, 2021, **31**, 2100380.

49 G. Zhou, X. Wang, H. Ji, J. Zhang, P. Kang, Z. Li and X. Xu, *J. Magn. Magn. Mater.*, 2020, **515**, 167303.

50 X. Han, J. Lee and H.-I. Yoo, *Phys. Rev. B:Condens. Matter Mater. Phys.*, 2009, **79**, 100403.

51 B. Ravel and M. Newville, *J. Synchrotron Radiat.*, 2005, **12**, 537.

52 G. Kresse and J. Furthmüller, *Comput. Mater. Sci.*, 1996, **6**, 15.

53 G. Kresse and D. Joubert, *Phys. Rev. B:Condens. Matter Mater. Phys.*, 1999, **59**, 1758.

54 J. P. Perdew, K. Burke and M. Ernzerhof, *Phys. Rev. Lett.*, 1997, **78**, 1396.

55 S. Grimme, S. Ehrlich and L. Goerigk, *J. Comput. Chem.*, 2011, **32**, 1456.

56 H. J. Monkhorst and J. D. Pack, *Phys. Rev. B*, 1976, **13**, 5188.